Article

Reconfigurable moiré nanolaser arrays with phase synchronization

https://doi.org/10.1038/s41586-023-06789-9

Received: 27 May 2023

Accepted: 26 October 2023

Published online: 13 December 2023

Check for updates

Hong-Yi Luan[1,4], Yun-Hao Ouyang[1,4], Zi-Wei Zhao[1,4], Wen-Zhi Mao[1] & Ren-Min Ma[1,2,3]✉

Miniaturized lasers play a central role in the infrastructure of modern information society. The breakthrough in laser miniaturization beyond the wavelength scale has opened up new opportunities for a wide range of applications[1–4], as well as for investigating light–matter interactions in extreme-optical-field localization and lasing-mode engineering[5–19]. An ultimate objective of microscale laser research is to develop reconfigurable coherent nanolaser arrays that can simultaneously enhance information capacity and functionality. However, the absence of a suitable physical mechanism for reconfiguring nanolaser cavities hinders the demonstration of nanolasers in either a single cavity or a fixed array. Here we propose and demonstrate moiré nanolaser arrays based on optical flatbands in twisted photonic graphene lattices, in which coherent nanolasing is realized from a single nanocavity to reconfigurable arrays of nanocavities. We observe synchronized nanolaser arrays exhibiting high spatial and spectral coherence, across a range of distinct patterns, including P, K and U shapes and the Chinese characters '中' and '国' ('China' in Chinese). Moreover, we obtain nanolaser arrays that emit with spatially varying relative phases, allowing us to manipulate emission directions. Our work lays the foundation for the development of reconfigurable active devices that have potential applications in communication, LiDAR (light detection and ranging), optical computing and imaging.

Moiré superlattices, resulting from the overlay of two periodic lattices with a twist or mismatched lattice constant, have garnered notable interest in the fields of electronics[20–26], photonics[27–37] and phononics[38–40]. The interlayer coupling induced by the reciprocal lattice vectors of a moiré superlattice provides a new degree of freedom for manipulating Bloch modes and customizing material properties. In electronic moiré superlattices, emergent phenomena including Hofstadter's butterfly[21,22], interfacial polarons[41] and moiré excitons[26] have been observed in van der Waals heterostructures. Of particular interest is the behaviour of bilayer graphene at a magic-angle twist, at which interlayer coupling induces flatbands with quenched quantum kinetic energy[20,23,24]. This phenomenon has been observed to result in correlated insulating and superconducting states[23,24]. Recent advancements in photonic moiré superlattices have also shown the emergence of flatbands, for which the properties of the system can be manipulated by twisting two photonic lattices[27–37].

Flatbands refer to the Bloch bands of periodic media that exhibit no dispersion. These bands possess fundamental compact localized states in real space that are highly degenerate and can exist not only within bandgaps but also within the continuum[30,42–48]. Notably, the degeneracy of these localized states enables any superposition of them to also be a static eigenstate of the system[42,44,46–48], offering an unprecedented avenue for developing reconfigurable optical devices with exceptional flexibility. However, this salient feature has only been realized in passive waveguiding systems[48]. In active systems, flatband-induced localization has only been used to achieve nanolasing in a single moiré unit cell[30]. In contrast to passive systems in which input laser beams control relative phases between different waveguides, phase locking in an active system arises spontaneously through mode coupling between different lasers, necessitating meticulous cavity design and precise experimental implementation.

Here we report a new type of moiré nanolaser array in which any desired pattern can be generated in an active structure, resulting not only in lasing but also ensuring that different lasing spots are in phase owing to the flatness of the band in momentum space. Our findings demonstrate that this approach provides an efficient means to create reconfigurable nanolaser arrays capable of phase locking, thereby enabling synchronized nanolasers across arrays with varying patterns (Fig. 1). The coherence of the moiré nanolaser array is confirmed by directional emission in far-field patterns and single-mode lasing in spatially resolved spectra. Furthermore, we demonstrate beam steering in moiré nanolaser arrays in which the emission directions are controlled by spatially varying relative phases of nanolasers.

Construction and operation mechanism

We construct a moiré nanolaser array based on optical flatbands in a nanostructured moiré superlattice, in which two sets of photonic

[1]State Key Laboratory for Mesoscopic Physics and Frontiers Science Center for Nano-optoelectronics, School of Physics, Peking University, Beijing, China. [2]Peking University Yangtze Delta Institute of Optoelectronics, Nantong, China. [3]National Biomedical Imaging Center, Peking University, Beijing, China. [4]These authors contributed equally: Hong-Yi Luan, Yun-Hao Ouyang, Zi-Wei Zhao. ✉e-mail: renminma@pku.edu.cn

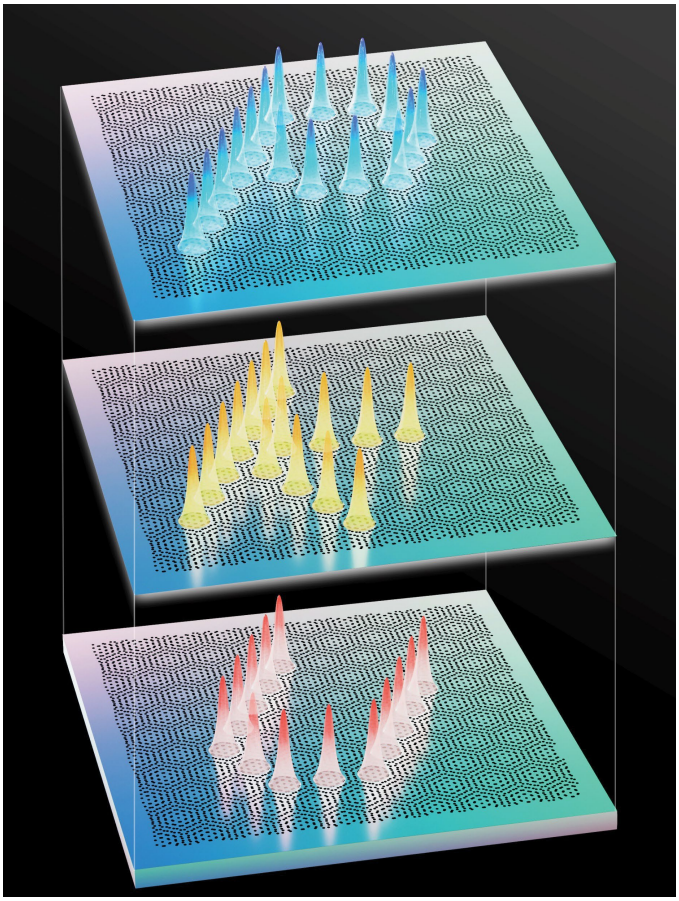

Fig. 1 | Reconfigurable moiré nanolaser array with phase locking. Schematic of the coherent reconfigurable moiré nanolaser that emits distinct patterns in the shapes of P (top layer), K (middle layer) and U (bottom layer). Each pattern is colour-coded to indicate the synchronization of constituent nanolasers in their emission phases. The nanolaser functions by exploiting the flatband mode localized at the centre of a single unit cell of the moiré superlattice as its resonant mode. Notably, the flatband degeneracy allows for an arbitrary superposition of localized flatband modes to serve as eigenmodes of the system. This crucial feature enables the creation of a reconfigurable nanolaser array, in which the resonant mode for reconfigurable nanolasing is determined by the flatband mode localized in a desired array of unit cells.

graphene lattices with a twist are introduced into the same semiconductor membrane of multiple quantum wells (MQWs; see Methods, Extended Data Fig. 1 and Supplementary Information Fig. 1). The membrane is 200 nm thick. The twisted angle between the two twisted lattices is 9.43°. The lattice constant of the formed moiré superlattice is 3.041 μm. The periodicity of the moiré superlattice in real space generates moiré reciprocal lattice vectors, through which Bloch modes with different momenta in the twisted lattices can couple to each other. Such coupling results in moiré Bloch modes containing different wavevectors that form localized wavefunctions in real space and, correspondingly, the flatbands in the energy-band diagram (see Methods and Supplementary Information Fig. 2), which is in strong contrast to normal photonic crystals wherein Bloch modes are delocalized.

We verify the flatband-induced field localization by demonstrating nanolasing in a single unit cell of the constructed moiré superlattice. Under optical pumping, single-cavity nanolasing is observed with a strongly localized wavefunction in the centre of a single unit cell of the moiré superlattice (Extended Data Fig. 2). According to three-dimensional full-wave simulation, the dipole flatband mode localized in a single moiré unit cell has a mode volume of $0.016\lambda^3$ (see Methods and Supplementary Information Fig. 3). We choose the relatively large twisted angle of 9.43° to construct the moiré superlattice for a smaller lattice constant of the moiré superlattice. Although a moiré superlattice with a smaller twisted angle has a narrower bandwidth of flatbands (Supplementary Information Fig. 4), it will have a larger footprint and in-sync nanolasing is more fragile to fabrication defects.

The achievement of strongly localized lasing within a single moiré unit cell in our work signifies that the localized lasing mode is an eigenmode of the moiré superlattice (because a lasing mode should be an eigenmode of the system), thereby enabling its use as a building block for constructing coherent reconfigurable nanolaser arrays. We can denote Ψ_j to represent the lasing mode localized in the jth single moiré unit cell and it should be an eigenmode of the eigenvalue equation $\mathscr{H}\Psi_j = E_j\Psi_j$ of the moiré superlattice. Therefore, Ψ_j ($j = 1, 2, \ldots, N$; N the number of total moiré unit cells in the superlattice) can serve as a complete basis of the degenerate flatband modes.

Owing to the degeneracy of the flatband, any linear combination (superposition) of the flatband modes localized in n arbitrary shaped moiré unit cells should also be an eigenmode of the same superlattice (that is, $\mathscr{H}\Phi \equiv \mathscr{H}\sum_{j=1}^{n}\Psi_j = \sum_{j=1}^{n}E_j\Psi_j = E\sum_{j=1}^{n}\Psi_j \equiv E\Phi$, in which $E = E_1, E_2, \ldots, E_n$). The eigenmodes $\Phi = \sum_{j=1}^{n}\Psi_j$ are used for single-mode lasing across various distinct patterns.

Coherent U-shaped moiré nanolaser array

We first demonstrate a U-shaped moiré nanolaser array that features phase locking (Fig. 2). The structure consists of 17 unit cells arranged in a U-shape, forming a cavity whose eigenmode arises from the superposition of the localized dipole flatband modes of the constituent cells. Figure 2a–c shows scanning electron microscopy (SEM) images of the device. The profile of the U-shaped cavity is marked in orange in Fig. 2a. We selectively excite the cavity mode using a U-shaped pump laser beam at room temperature (Supplementary Information Figs. 5 and 6c).

Figure 2d shows the log-scale light–light curve and the second-order intensity correlation function $g^{(2)}(\tau = 0)$ evolution curve of the nanolaser array. The S-shaped log-scale light–light curve indicates the phase transition from spontaneous emission to stimulated emission, with the lasing threshold set at 9.8 kW cm^{-2} based on the quantum threshold definition (inset of Fig. 2d). As the pump power increases beyond the threshold, the linewidth of the cavity mode sharply reduces (Extended Data Fig. 3a,b). The lasing is further confirmed by $g^{(2)}(\tau)$ characterization of the nanolaser array (Fig. 2d and Extended Data Fig. 3c,d). Near the lasing threshold, the emitted photons exhibit super-Poissonian light characteristics ($g^{(2)}(\tau = 0) > 1$). Above the lasing threshold, the photon-emission statistics transition from super-Poissonian to Poissonian, indicating the emergence of coherent light emission ($g^{(2)}(\tau = 0) = 1$). As we decrease pump power below the threshold, we observe a decline in measured values for $g^{(2)}(\tau = 0)$, which is because of a reduction in coherence length of spontaneous emission approaching close proximity to the temporal resolution limit (100 ps) imposed by our measurement set-up.

The spontaneous emission patterns of the U-shaped moiré nanolaser array are presented in Fig. 2e,f in real and momentum spaces, respectively. In real space, the pattern is determined by the shape of the pump laser beam and the centres of the unit cells stand out as slightly brighter spots owing to their higher local density of states (Fig. 2e). By contrast, in momentum space, the emission is evenly distributed across the imaging area, reflecting the omnidirectional nature of spontaneous emission (Fig. 2f). Figure 2k shows the spectrum of the spontaneous emission well below the lasing threshold.

Once the lasing threshold is surpassed, the patterns in real and momentum spaces undergo a pronounced change, exhibiting coherent features (Fig. 2g,h). In particular, the emission in real space becomes predominantly localized at the centres of each unit cell, indicating that the flatband can effectively localize the cavity mode within a single moiré unit cell, both horizontally and vertically, in a desired pattern

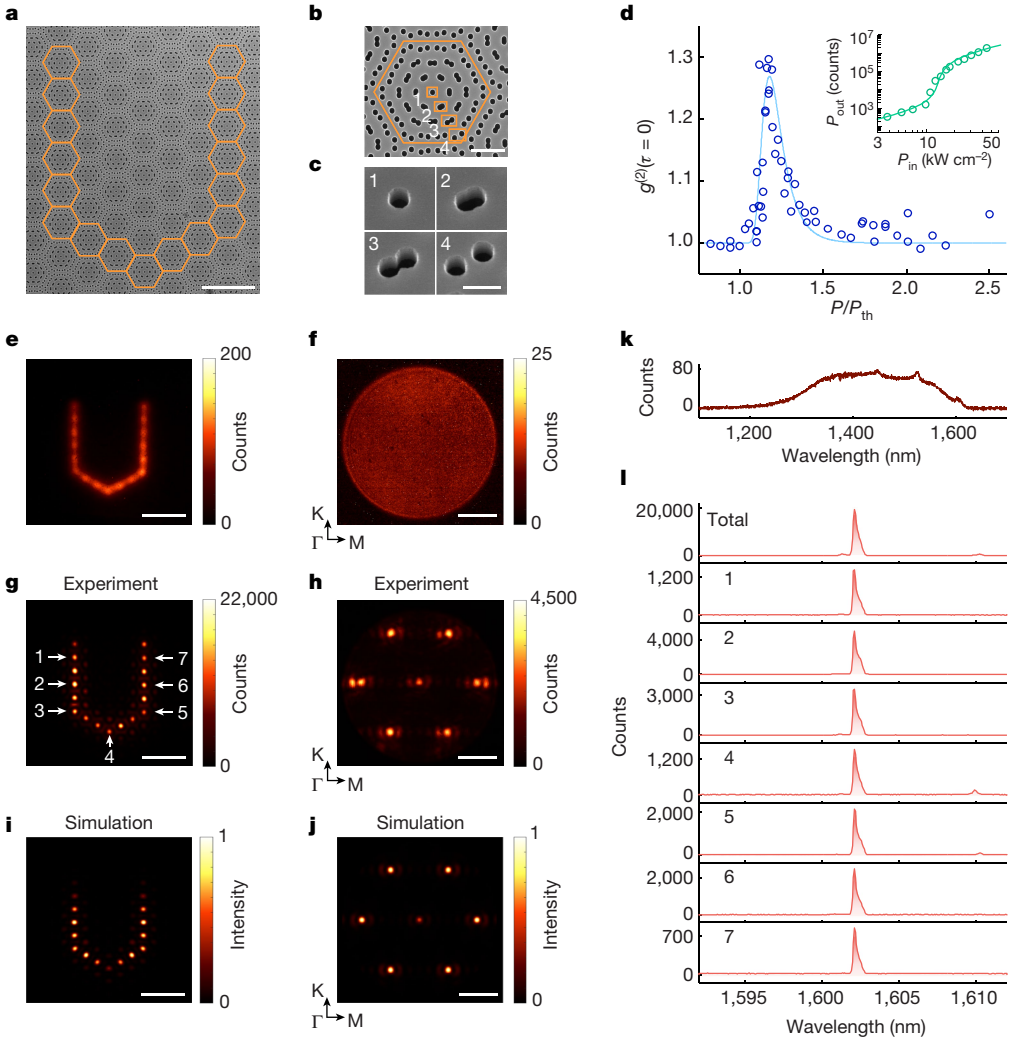

Fig. 2 | U-shaped moiré nanolaser array with phase locking. a, SEM image of the U-shaped moiré nanolaser composed of 17 unit cells of the moiré superlattice highlighted by orange hexagons. The moiré superlattice is fabricated in a semiconductor membrane consisting of InGaAsP MQWs. Scale bar, 5 μm. **b**, Enlarged SEM image highlighting a single unit cell of the moiré superlattice. Scale bar, 1 μm. **c**, Perspective-view SEM images of the four designated areas in **b**, which depict the distinct layers of MQWs. Scale bar, 300 nm. **d**, Second-order intensity correlation function $g^{(2)}(\tau = 0)$ of the nanolaser array, exhibiting super-Poissonian light characteristics ($g^{(2)}(\tau = 0) > 1$) in the vicinity of the lasing threshold. Above the lasing threshold, the emitted photons become coherent and their statistics shift from super-Poissonian to Poissonian ($g^{(2)}(\tau = 0) = 1$). Circles, data; line, guide to the eye. Inset, light–light curve of the U-shaped moiré nanolaser array on a logarithmic scale, presenting lasing threshold behaviour of the array. Circles, data; line, fitting. **e**,**f**, Spontaneous emission patterns of the U-shaped moiré nanolaser array in real (**e**) and momentum (**f**) spaces. Scale bars, 10 μm (**e**), 1.6 μm^{-1} (**f**). **g**,**h**, Lasing emission patterns of the U-shaped moiré nanolaser array in real (**g**) and momentum (**h**) spaces. Scale bars, 10 μm (**g**), 1.6 μm^{-1} (**h**). **i**,**j**, Simulated emission patterns in real (**i**) and momentum (**j**) spaces, which match well with the experimental ones in **g** and **h**. Scale bars, 10 μm (**i**), 1.6 μm^{-1} (**j**). **k**, Spontaneous emission spectrum of the U-shaped moiré nanolaser array. **l**, Spectrum of the entire U-shaped moiré nanolaser array (top spectrum) and spatially resolved spectra from seven individual unit cells marked in **g**.

(Fig. 2g). To confirm the spectral coherence of the array, we conducted spatially resolved spectroscopy (Fig. 2l). The spectrum of the entire U-shaped moiré nanolaser array shows a single lasing mode at approximately 1,602 nm, with a full width at half maximum of 0.32 nm (top spectrum of Fig. 2l). Figure 2l also shows spatially resolved emission spectra from seven individual unit cells, all of which exhibit the same properties in terms of emission wavelength and full width at half maximum as the spectrum of the full array.

In momentum space, omnidirectional spontaneous emission transforms into directional emission emanating from seven Γ points of the moiré superlattice within the light cone. The distance between adjacent Γ points is about $2.31\pi/A$, in which A is the lattice constant of the moiré superlattice. At each Γ point, the main lobe has a divergence angle of about 8.1°. This directional emission is the outcome of the in-phase collective lasing of all the localized nanolasers in the U-shaped cavity. Figure 2i,j shows the simulated emission patterns in real and momentum spaces, respectively, which are obtained by three-dimensional full-wave simulation (see Methods). All of the dipole flatband modes of the 17 unit cells in the simulation have the same emission phase (Extended Data Fig. 4). The resulting emission patterns in both real and momentum spaces match well with the experimental ones. The side lobes in the momentum-space pattern arise from the interreference of the coherent emissions originating from the left and right vertical lines of the U-shaped nanolaser array, respectively. The separation between the vertical lines measures roughly 15.80 μm, which corresponds to an interference pattern in momentum space with fringes spaced at 0.398 μm^{-1}, matching well with the experimental observed value of 0.391 μm^{-1}.

The moiré reciprocal lattice vectors scatter the flatband mode into the light cone, allowing for lasing radiation into free space. In comparison with the six Γ point beams on the sides, because of its larger

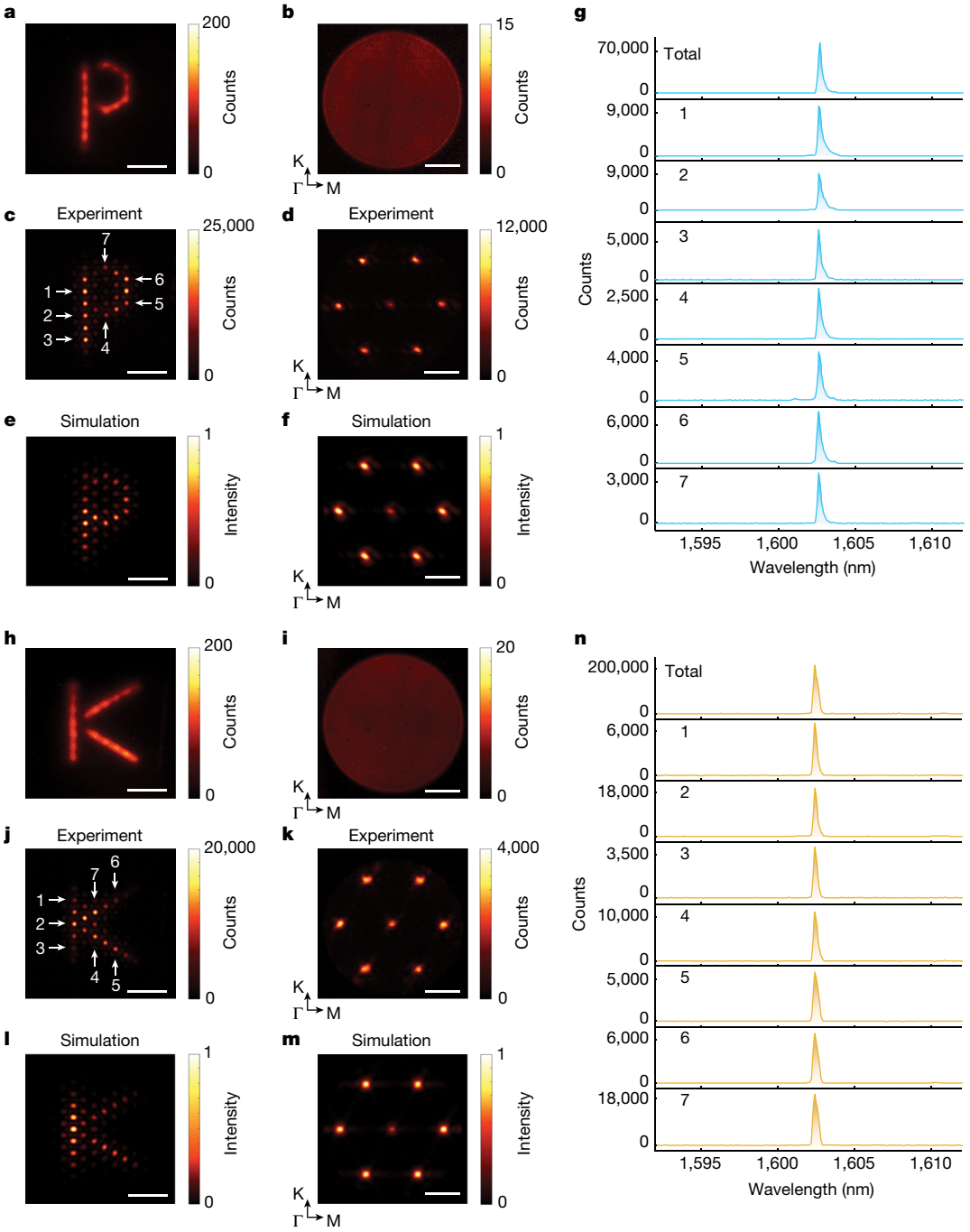

Fig. 3 | Coherent P-shaped and K-shaped moiré nanolaser arrays. **a**,**b**, Spontaneous emission patterns of the P-shaped moiré nanolaser array in real (**a**) and momentum (**b**) spaces. Scale bars, 10 μm (**a**), 1.6 μm^{-1} (**b**). **c**,**d**, Lasing emission patterns of the array in real (**c**) and momentum (**d**) spaces. Scale bars, 10 μm (**c**), 1.6 μm^{-1} (**d**). **e**,**f**, Simulated emission patterns in real (**e**) and momentum (**f**) spaces, which match well with the experimental ones in **c** and **d**. Scale bars, 10 μm (**e**), 1.6 μm^{-1} (**f**). **g**, Spectrum of the entire P-shaped moiré nanolaser array (top spectrum) and spatially resolved spectra from seven individual unit cells marked in **c**. **h**,**i**, Spontaneous emission patterns of the K-shaped moiré nanolaser array in real (**h**) and momentum (**i**) spaces. Scale bars, 10 μm (**h**), 1.6 μm^{-1} (**i**). **j**,**k**, Lasing emission patterns of the array in real (**j**) and momentum (**k**) spaces. Scale bars, 10 μm (**j**), 1.6 μm^{-1} (**k**). **l**,**m**, Simulated emission patterns in real (**l**) and momentum (**m**) spaces, which match well with the experimental ones in **j** and **k**. Scale bars, 10 μm (**l**), 1.6 μm^{-1} (**m**). **n**, Spectrum of the entire K-shaped moiré nanolaser array (top spectrum) and spatially resolved spectra from seven individual unit cells marked in **j**.

distance from the dominant momentum of lasing Bloch mode, scattering towards the centre Γ point beam is less efficient, resulting in stronger intensities observed at those six Γ point beams.

Achieving coherent reconfigurability, that is, ensuring that all constituent nanolasers in the array emit in phase and at the same frequency and polarization (Extended Data Fig. 5), necessitates a deterministic relationship between patterns in real space, patterns in momentum space and the presence of flatband modes (Extended Data Fig. 6). The lasing patterns observed in real space and momentum space can be mutually transformed through Fourier transform. The lasing pattern observed in momentum space provides information about the eigenfrequency distribution determined by the dispersion relation (band structure), which should exhibit high degeneracy to enable single-mode lasing, meaning that the band structure needs to be flat enough.

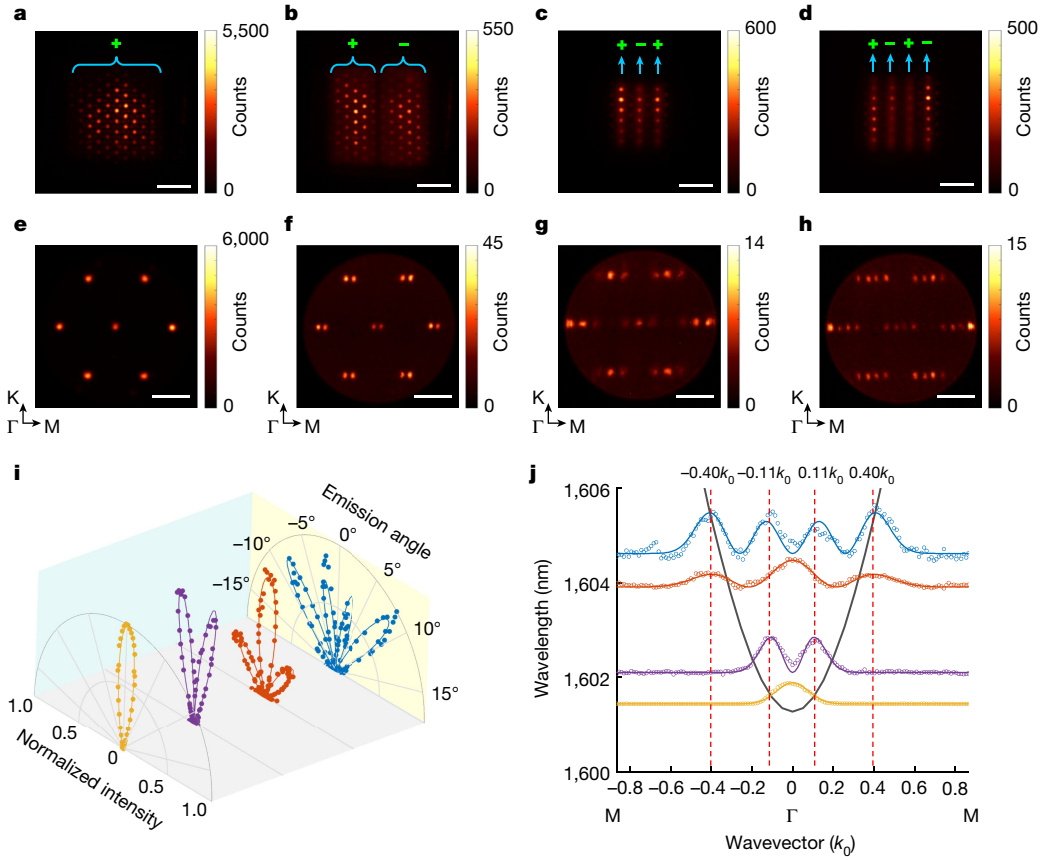

Fig. 4 | Phase-dependent superposition for beam steering. a–**d**, Lasing emission patterns of the fundamental (**a**), first higher (**b**), second higher (**c**) and third higher (**d**) modes that have 0, 1, 2 and 3 nodes in the horizontal direction, respectively. In the fundamental mode, all constituent nanolasers in the array emit with synchronized phases. However, for the first, second and third higher modes, a phase difference of π exists between every two adjacent areas marked with '+' and '−' signs. Scale bars, 10 μm. **e**–**h**, Momentum-space lasing emission patterns of the fundamental (**e**), first higher (**f**), second higher (**g**) and third higher (**h**) modes. Scale bars, 1.6 μm^{-1}. **i**, Angle-resolved intensity profiles of the four spatial modes at the central Γ point in the horizontal direction. Dots, data; lines, fitting. **j**, Three-dimensional full-wave-simulated band diagram of the flatband along the Γ–M direction, accompanied by superimposed momentum distributions of four modes, as depicted in **a**–**d**. The value at the M point of each curve, measured along the vertical axis, represents the resonant wavelength of the mode. The group refractive indices at the resonant wavelengths of the four modes are 130, 58, 37 and 32, respectively. Dots, data; lines, fitting.

As a control experiment, we have further demonstrated an incoherent reconfigurability U-shaped nanolaser array (Extended Data Fig. 7), in which the reconfigurability is solely represented in real space. Although the real-space pattern exhibits similarities to the coherent one presented in Fig. 2g, notable distinctions can be observed in both momentum-space pattern and spectrum. The incoherent reconfigurable array demonstrates a larger divergence angle similar to that from a single moiré unit cell (Extended Data Fig. 2g) and several lasing modes (different nanolasers in the array emit at different frequencies).

Reconfiguring moiré nanolaser array

We now reconfigure the moiré nanolaser array into P and K shapes using P-shaped and K-shaped pump laser beams, respectively (Fig. 3 and Supplementary Information Fig. 6a,b). The log-scale light–light curves and the linewidth evolution curves of the P-shaped and K-shaped moiré nanolaser arrays are shown in Supplementary Information Fig. 7, which exhibit similar threshold and linewidth narrowing behaviours as the U-shaped array. Below the lasing threshold, the emission patterns of the P-shaped and K-shaped moiré nanolaser arrays show typical features of spontaneous emission, with the real-space patterns defined by the pump laser beams and the momentum-space patterns showing omnidirectional emission (Fig. 3a,b and Fig. 3h,i).

Figure 3c,d (Fig. 3j,k) shows the lasing emission pattern of the P-shaped (K-shaped) moiré nanolaser array in real and momentum spaces, respectively. The in-phase collective lasing of the nanolaser arrays is also verified by single-mode lasing in spatially resolved spectroscopy (Fig. 3g,n) and directional emission in far-field beam patterns (Fig. 3d,k). Figure 3e,f (Fig. 3l,m) shows the simulated emission patterns in real and momentum spaces, respectively, for the P-shaped (K-shaped) moiré nanolaser array, which match well with the experimental ones.

Beam steering of moiré nanolaser array

To manipulate the radiation direction of a moiré nanolaser array, we use a phased-array approach that relies on the superposition of flatband localized modes with different relative phases. The wavefunctions in this scenario can be written as $\Phi' = \sum_{j=1}^{m} \Psi_j + \sum_{j=m+1}^{2m}(-\Psi_j) + \sum_{j=2m+1}^{3m} \Psi_j + \sum_{j=3m+1}^{4m}(-\Psi_j) + \ldots$, in which the terms with a minus sign in Φ' represent a π phase difference compared with the other terms. The constant phase differences between neighbouring columns result in the directional control of beam steering.

The in-phase collective lasing of a nanolaser array is linked to the Bloch momentum of its cavity mode around the Γ point. The phase-dependent superposition requires the excitation of a cavity mode with higher Bloch momentum, located away from the Γ point. This higher Bloch momentum mode has a node (intensity zero crossing) in real space and, therefore, can be selectively excited using pump beams with similar intensity distributions (Supplementary Information Fig. 6d–g).

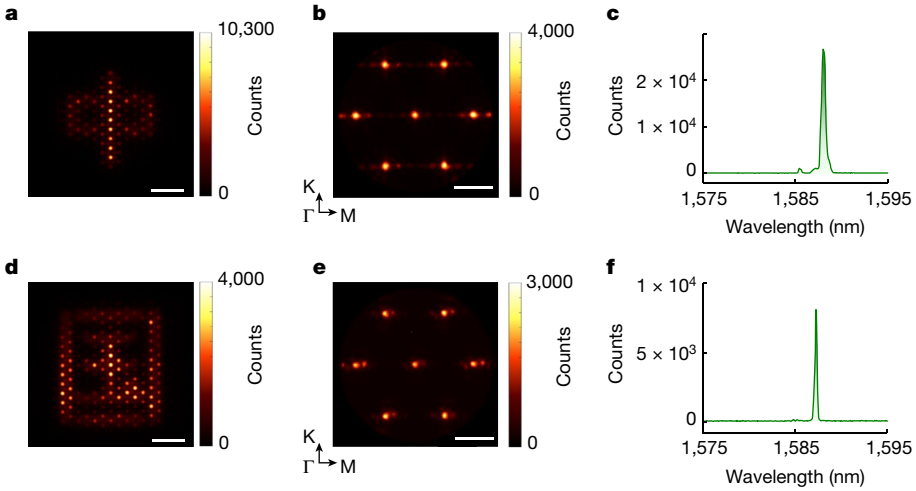

Fig. 5 | Coherent reconfigurable moiré nanolaser arrays in the Chinese characters '中' and '国' ('China' in Chinese). a–**c**, Real-space pattern (**a**), momentum-space pattern (**b**) and lasing spectrum (**c**) of the Chinese character '中'. Scale bars, 10 μm (**a**), 1.6 μm^{-1} (**b**). **d**–**f**, Real-space pattern (**d**), momentum-space pattern (**e**) and lasing spectrum (**f**) of the Chinese character '国'. Scale bars, 10 μm (**d**), 1.6 μm^{-1} (**e**).

Figure 4a,b shows the lasing emission patterns of two moiré nanolaser arrays with Bloch momenta centred at the Γ point and at $\pm 0.11k_0$, respectively, in which k_0 denotes the side length of the moiré Brillouin zone. These are the fundamental and first higher modes exhibiting 0 and 1 nodes in the Γ–M direction, respectively (Extended Data Fig. 8i,j). Figure 4c,d shows the lasing emission patterns of two arrays with Bloch momentum both centred at $\pm 0.40k_0$, in which the next-nearest-neighbour nanolasers in the Γ–M direction have a π phase difference (Extended Data Fig. 8k,l). These two modes have 2 and 3 nodes in the Γ–M direction and can be denoted as the second and third higher modes, respectively.

The different spatial phases result in varied lasing emission directions. Figure 4e–h depicts the lasing emission patterns of those four modes in momentum space, in which their Bloch momenta are clearly resolved. As well as short-wavelength components, the second and third higher modes also contain long-wavelength components with momenta centred at the Γ point and at $\pm\frac{1}{3} \times 0.40k_0$. These long-wavelength components modify the lasing emission patterns, resulting in stronger intensity side columns for both modes (Fig. 4c,d). Figure 4i presents the angle-resolved intensity profiles of the four spatial modes at the central Γ point in the horizontal direction, at which effective steering is clearly illustrated. By conducting three-dimensional full-wave simulations, we have computed the emission patterns in both real and momentum spaces for all four modes illustrated in Fig. 4, which exhibit strong agreement with experimental observations (Extended Data Fig. 8).

Slow light in the flatband

The flatband exhibits slow light, as indicated by its energy-band diagram and the measured wavelength–momentum relations of the four modes (Fig. 4j). Specifically, at the resonant wavelengths of the four modes, the group velocity is substantially slowed down to 0.76%, 1.7%, 2.7% and 3.1% of the speed of light in vacuum, respectively. The corresponding group refractive indices of these modes are about 130, 58, 37 and 32, respectively. In the experiment, we observe that the threshold of the single-cavity nanolaser is much higher compared with that of the nanolaser array depicted in Fig. 4a (Supplementary Information Fig. 8), emphasizing the importance of reducing speed in achieving low-threshold lasing, as the momentum distribution of the array closely approaches the Γ point. In future research, a smaller twisted angle can be used to further decrease the group velocity of localized Bloch modes in moiré superlattices, enabling the exploration of more intriguing stopped-wave phenomena[30,32,49,50]. In Supplementary Information Table 1, we provide a comparison of key laser merits, including threshold, lasing quality factor and mode volume, with other state-of-the-art microscale lasers. We note that, owing to its high quality factor, these nanolasers can be electrically pumped at room temperature with the introduction of an appropriate electrical interface.

The reduced velocity and increased group index are a direct consequence of the flatness of the band, which naturally associates with the localization of the field. Notably, the flatband has a bandwidth of only about 2 THz within the moiré Brillouin zone, which is much narrower than other normal bands (Extended Data Fig. 9). The narrow bandwidth lays the foundation for the development of the demonstrated reconfigurable phase-locked nanolaser arrays. If the moiré nanolaser array deviates from exact periodicity, different quasi-moiré unit cells will exhibit distinct structures and therefore possess varying resonant frequencies. Although it remains feasible to realize a nanolaser array in real space, achieving coherent emission from an array becomes unattainable (Supplementary Information Fig. 9).

Scalability of the moiré nanolaser array

The synchronization of emission in the moiré nanolaser array relies on the flatness of the band structure in momentum space. In our experiment, we use a moiré superlattice with a predetermined twisted angle to ensure the required periodicity for forming a flatband (see Methods). This characteristic enables scalability of the moiré nanolaser array. However, practical limitations may arise owing to nonuniformities induced during the fabrication process when realizing large-scale moiré nanolaser arrays.

To enhance the uniformity of the fabricated moiré superlattices, we bond the membrane containing the superlattices onto a SiO_2 substrate. This step eliminates any deformations that may arise from suspending the membrane. Through this process, more than 160 nanolasers are synchronized to achieve single-mode lasing with high spatial and spectral coherence (Extended Data Fig. 10). As a result of the increased coherence area, the scaled-up moiré nanolaser array has a divergence angle of only about 3°. By using the high uniformity of large-scale moiré superlattices, we successfully realize coherent reconfigurable nanolaser arrays in more intricate patterns, such as the Chinese characters '中' and '国' ('China' in Chinese) as shown in Fig. 5.

Summary

In this work, we have proposed and demonstrated a moiré nanolaser array that exploits the superposition properties of flatbands to create reconfigurable active photonic devices. We verify the field localization induced by the flatband through nanolasing from a single moiré unit cell, the strong field localization of the nanolaser arrays in both horizontal and vertical directions, as well as the slow light at a group refractive index of more than 100. We demonstrate the effectiveness of our approach by realizing reconfigurable moiré nanolaser arrays in various patterns, including P, K and U shapes and the Chinese characters '中' and '国', while maintaining high spatial and spectral coherence. Furthermore, by constructing phase-dependent superpositions of the flatband localized modes, we demonstrate phased-array nanolasers capable of steering radiation directions. Our results offer a promising path towards constructing complex phased-array nanolasers for communication, computing and spectroscopy applications.

Online content

Any methods, additional references, Nature Portfolio reporting summaries, source data, extended data, supplementary information, acknowledgements, peer review information; details of author contributions and competing interests; and statements of data and code availability are available at https://doi.org/10.1038/s41586-023-06789-9.

1. Berini, P. & De Leon, I. Surface plasmon–polariton amplifiers and lasers. *Nat. Photon.* **6**, 16–24 (2012).
2. Hill, M. T. & Gather, M. C. Advances in small lasers. *Nat. Photon.* **8**, 908–918 (2014).
3. Eaton, S. W., Fu, A., Wong, A. B., Ning, C. Z. & Yang, P. Semiconductor nanowire lasers. *Nat. Rev. Mater.* **1**, 16028 (2016).
4. Ma, R.-M. & Oulton, R. F. Applications of nanolasers. *Nat. Nanotechnol.* **14**, 12–22 (2019).
5. Bandres, M. A. et al. Topological insulator laser: experiments. *Science* **359**, eaar4005 (2018).
6. Ha, S. T. et al. Directional lasing in resonant semiconductor nanoantenna arrays. *Nat. Nanotechnol.* **13**, 1042–1047 (2018).
7. Yoshida, M. et al. Double-lattice photonic-crystal resonators enabling high-brightness semiconductor lasers with symmetric narrow-divergence beams. *Nat. Mater.* **18**, 121–128 (2019).
8. Carlon Zambon, N. et al. Optically controlling the emission chirality of microlasers. *Nat. Photon.* **13**, 283–288 (2019).
9. Zeng, Y. et al. Electrically pumped topological laser with valley edge modes. *Nature* **578**, 246–250 (2020).
10. Shao, Z. K. et al. A high-performance topological bulk laser based on band-inversion-induced reflection. *Nat. Nanotechnol.* **15**, 67–72 (2020).
11. Yang, Z. Q., Shao, Z. K., Chen, H. Z., Mao, X. R. & Ma, R. M. Spin-momentum-locked edge mode for topological vortex lasing. *Phys. Rev. Lett.* **125**, 013903 (2020).
12. Huang, C. et al. Ultrafast control of vortex microlasers. *Science* **367**, 1018–1021 (2020).
13. Dikopoltsev, A. et al. Topological insulator vertical-cavity laser array. *Science* **373**, 1514–1517 (2021).
14. Contractor, R. et al. Scalable single-mode surface-emitting laser via open-Dirac singularities. *Nature* **608**, 692–698 (2022).
15. Zhang, Z. et al. Spin–orbit microlaser emitting in a four-dimensional Hilbert space. *Nature* **612**, 246–251 (2022).
16. Yang, L. et al. Topological-cavity surface-emitting laser. *Nat. Photon.* **16**, 279–283 (2022).
17. Schumer, A. et al. Topological modes in a laser cavity through exceptional state transfer. *Science* **375**, 884–888 (2022).
18. Sang, Y. G. et al. Topological polarization singular lasing with highly efficient radiation channel. *Nat. Commun.* **13**, 6485 (2022).
19. Chen, Y. et al. Compact spin-valley-locked perovskite emission. *Nat. Mater.* **22**, 1065–1070 (2023).
20. Bistritzer, R. & MacDonald, A. H. Moiré bands in twisted double-layer graphene. *Proc. Natl Acad. Sci. USA* **108**, 12233–12237 (2011).
21. Dean, C. R. et al. Hofstadter's butterfly and the fractal quantum Hall effect in moiré superlattices. *Nature* **497**, 598–602 (2013).
22. Ponomarenko, L. A. et al. Cloning of Dirac fermions in graphene superlattices. *Nature* **497**, 594–597 (2013).
23. Cao, Y. et al. Correlated insulator behaviour at half-filling in magic-angle graphene superlattices. *Nature* **556**, 80–84 (2018).
24. Cao, Y. et al. Unconventional superconductivity in magic-angle graphene superlattices. *Nature* **556**, 43–50 (2018).
25. Kennes, D. M. et al. Moiré heterostructures as a condensed-matter quantum simulator. *Nat. Phys.* **17**, 155–163 (2021).
26. Huang, D., Choi, J., Shih, C.-K. & Li, X. Excitons in semiconductor moiré superlattices. *Nat. Nanotechnol.* **17**, 227–238 (2022).
27. Sunku, S. S. et al. Photonic crystals for nano-light in moiré graphene superlattices. *Science* **362**, 1153–1156 (2018).
28. Hu, G. et al. Topological polaritons and photonic magic angles in twisted α-MoO_3 bilayers. *Nature* **582**, 209–213 (2020).
29. Wang, P. et al. Localization and delocalization of light in photonic moiré lattices. *Nature* **577**, 42–46 (2020).
30. Mao, X. R., Shao, Z. K., Luan, H. Y., Wang, S. L. & Ma, R. M. Magic-angle lasers in nanostructured moiré superlattice. *Nat. Nanotechnol.* **16**, 1099–1105 (2021).
31. Dong, K. et al. Flat bands in magic-angle bilayer photonic crystals at small twists. *Phys. Rev. Lett.* **126**, 223601 (2021).
32. Ma, R. M. et al. Twisted lattice nanocavity with theoretical quality factor exceeding 200 billion. *Fundam. Res.* **3**, 537–543 (2023).
33. Wang, H., Ma, S., Zhang, S. & Lei, D. Intrinsic superflat bands in general twisted bilayer systems. *Light Sci. Appl.* **11**, 159 (2022).
34. Meng, Z. et al. Atomic Bose–Einstein condensate in twisted-bilayer optical lattices. *Nature* **615**, 231–236 (2023).
35. Du, L. et al. Moiré photonics and optoelectronics. *Science* **379**, eadg0014 (2023).
36. Guan, J. et al. Far-field coupling between moiré photonic lattices. *Nat. Nanotechnol.* **18**, 514–520 (2023).
37. Tang, H. et al. Experimental probe of twist angle–dependent band structure of on-chip optical bilayer photonic crystal. *Sci. Adv.* **9**, eadh8498 (2023).
38. Zheng, Z. et al. Phonon polaritons in twisted double-layers of hyperbolic van der Waals crystals. *Nano Lett.* **20**, 5301–5308 (2020).
39. Duan, J. et al. Twisted nano-optics: manipulating light at the nanoscale with twisted phonon polaritonic slabs. *Nano Lett.* **20**, 5323–5329 (2020).
40. Chen, M. et al. Configurable phonon polaritons in twisted α-MoO_3. *Nat. Mater.* **19**, 1307–1311 (2020).
41. Chen, C. et al. Emergence of interfacial polarons from electron–phonon coupling in graphene/h-BN van der Waals heterostructures. *Nano Lett.* **18**, 1082–1087 (2018).
42. Sutherland, B. Localization of electronic wave functions due to local topology. *Phys. Rev. B* **34**, 5208–5211 (1986).
43. Arai, M., Tokihiro, T., Fujiwara, T. & Kohmoto, M. Strictly localized states on a two-dimensional Penrose lattice. *Phys. Rev. B* **38**, 1621–1626 (1988).
44. Guzmán-Silva, D. et al. Experimental observation of bulk and edge transport in photonic Lieb lattices. *New J. Phys.* **16**, 063061 (2014).
45. Mukherjee, S. et al. Observation of a localized flat-band state in a photonic Lieb lattice. *Phys. Rev. Lett.* **114**, 245504 (2015).
46. Vicencio, R. A. et al. Observation of localized states in Lieb photonic lattices. *Phys. Rev. Lett.* **114**, 245503 (2015).
47. Xia, S. et al. Unconventional flatband line states in photonic Lieb lattices. *Phys. Rev. Lett.* **121**, 263902 (2018).
48. Tang, L. et al. Photonic flat-band lattices and unconventional light localization. *Nanophotonics* **9**, 1161–1176 (2020).
49. Tsakmakidis, K. L., Pickering, T. W., Hamm, J. M., Page, A. F. & Hess, O. Completely stopped and dispersionless light in plasmonic waveguides. *Phys. Rev. Lett.* **112**, 167401 (2014).
50. Tsakmakidis, K. L., Hess, O., Boyd, R. W. & Zhang, X. Ultraslow waves on the nanoscale. *Science* **358**, eaan5196 (2017).

Methods

Device fabrication

We use InGaAsP MQWs with a thickness of 200 nm as the semiconductor membrane to fabricate moiré superlattices. The nanostructured MQWs function as both photonic crystals and gain materials for lasing. We use a single pattern file comprising two sets of nanoholes with a predetermined twisted angle, which is incorporated during the CAD pattern drawing process. Subsequently, we conduct electron-beam lithography once to transfer the pattern onto the electron-beam resist and use the inductively coupled plasma (ICP) etching technique to fabricate the designed microstructure into a MQWs membrane. The InP substrate of the MQWs is removed using a wet etching method with a HCl:H_2O (3:1) solution to form the final suspended membrane featuring moiré superlattices.

Theoretical analysis of moiré superlattices

The periodicity of the moiré superlattice induces reciprocal lattice vectors, which couple Bloch modes of twisted photonic graphene lattices and form localized eigenmodes at the centre of each unit cell. We theoretically analyse this field-localization mechanism using a tight-binding model.

We begin by solving the band structure of a single-layer photonic graphene lattice, using Bloch waves situated at nonequivalent A and B sites ($|A_\mathbf{k}\rangle$ and $|B_\mathbf{k}\rangle$) of the lattice as the basis to construct the Hamiltonian, in which $\mathbf{k}$ is set as the wavevector of the basis. Subsequently, the Hamiltonian of the single-layer photonic graphene lattice can be expressed as,

$$\mathscr{H}(\mathbf{k}) = \begin{pmatrix} \langle A_\mathbf{k}|\mathscr{H}(\mathbf{r})|A_\mathbf{k}\rangle & \langle A_\mathbf{k}|\mathscr{H}(\mathbf{r})|B_\mathbf{k}\rangle \\ \langle B_\mathbf{k}|\mathscr{H}(\mathbf{r})|A_\mathbf{k}\rangle & \langle B_\mathbf{k}|\mathscr{H}(\mathbf{r})|B_\mathbf{k}\rangle \end{pmatrix}. \tag{1}$$

The two diagonal elements are equal to f_0, whereas the two non-diagonal coupling terms have the following form:

$$\langle A_\mathbf{k}|\mathscr{H}(\mathbf{r})|B_\mathbf{k}\rangle = J\left(e^{i\mathbf{k}\cdot\boldsymbol{\tau}_A} + e^{-i\mathbf{k}\cdot\boldsymbol{\tau}_B} + e^{i\mathbf{k}\cdot(\boldsymbol{\tau}_B-\boldsymbol{\tau}_A)}\right), \tag{2}$$

in which J is the coupling coefficient between the A and B sites and $\boldsymbol{\tau}_A = \frac{a}{2\sqrt{3}}(-1, \sqrt{3})$, $\boldsymbol{\tau}_B = \frac{a}{2\sqrt{3}}(1, \sqrt{3})$, with a being the length of the lattice constant of the photonic graphene lattice. By solving the eigenequation, we can obtain the band structure containing two Dirac cones at K and K′ points as,

$$f(\mathbf{k}) = f_0 \pm J\sqrt{3 + 2\cos[\mathbf{k}\cdot\boldsymbol{\tau}_A] + 2\cos[\mathbf{k}\cdot\boldsymbol{\tau}_B] + 2\cos[\mathbf{k}\cdot(\boldsymbol{\tau}_B - \boldsymbol{\tau}_A)]}\,.$$

By introducing a second set of photonic graphene lattices to the first one with a twist, a moiré superlattice is formed with moiré periodicity. The resulting moiré reciprocal lattice vectors can be expressed by $\pm(\mathbf{G}^{(1)} - \mathbf{G}^{(2)})$, in which $\mathbf{G}^{(1)}$ and $\mathbf{G}^{(2)}$ are the reciprocal lattice vectors of the first and second set of photonic graphene lattices, respectively. The moiré reciprocal lattice vectors enable the couplings of Bloch modes in photonic graphene lattices under momentum conservation. This coupling can lead to localized eigenfunctions at the centre of each unit cell of the moiré superlattice, which contain different wavevectors. These localized eigenfunctions are Bloch modes within the flatband of the moiré superlattice.

We analytically solve the wavefunctions of the flatband modes by considering Bloch modes involved in coupling throughout the Brillouin zone of a single-layer photonic graphene lattice. Within this range, the total number of Bloch modes that satisfy momentum conservation and are involved in the coupling is 148. We construct the 148 Bloch modes by using Wannier functions $W_{A,B}(\mathbf{r})$ situated at the A and B sites, which are:

$$\begin{cases} |A_{\mathbf{k}_j}^{(\alpha)}\rangle = \dfrac{1}{\sqrt{N}}\sum_n e^{i\mathbf{k}_j\cdot(\mathbf{R}_n^{(\alpha)}+\boldsymbol{\tau}_A^{(\alpha)})} W_A^{(\alpha)}(\mathbf{r} - (\mathbf{R}_n^{(\alpha)} + \boldsymbol{\tau}_A^{(\alpha)})) \\ |B_{\mathbf{k}_j}^{(\alpha)}\rangle = \dfrac{1}{\sqrt{N}}\sum_n e^{i\mathbf{k}_j\cdot(\mathbf{R}_n^{(\alpha)}+\boldsymbol{\tau}_B^{(\alpha)})} W_B^{(\alpha)}(\mathbf{r} - (\mathbf{R}_n^{(\alpha)} + \boldsymbol{\tau}_B^{(\alpha)})) \end{cases}, \tag{3}$$

in which $|A_{\mathbf{k}_j}^{(\alpha)}\rangle$ and $|B_{\mathbf{k}_j}^{(\alpha)}\rangle$ are Bloch modes at the A and B sites of the first ($\alpha = 1$) and second ($\alpha = 2$) set of lattices with wavevector $\mathbf{k}_j$, respectively. $\mathbf{R}_n$ is summed over the triangular Bravais lattice. $\mathbf{k}_j$ ($j = 1, 2, \ldots, 37$) are wavevectors differed by moiré reciprocal lattice vectors throughout the first Brillouin zone of the first set of photonic graphene lattices.

The corresponding Hamiltonian is

$$\mathscr{H}_{\text{twisted}} = \begin{pmatrix} \mathscr{H}_1 & \kappa \\ \kappa^\dagger & \mathscr{H}_2 \end{pmatrix}, \tag{4}$$

in which

$$\begin{aligned} \mathscr{H}_1 &= \text{Diag}(\mathscr{H}^{(1)}(\mathbf{k}_1), \mathscr{H}^{(1)}(\mathbf{k}_2), \ldots, \mathscr{H}^{(1)}(\mathbf{k}_{37})) \\ \mathscr{H}_2 &= \text{Diag}(\mathscr{H}^{(2)}(\mathbf{k}_1), \mathscr{H}^{(2)}(\mathbf{k}_2), \ldots, \mathscr{H}^{(2)}(\mathbf{k}_{37})) \end{aligned} \tag{5}$$

are the Hamiltonians of the two sets of lattices, respectively, and κ is the interlattice coupling matrix, which can be expressed as

$$\kappa = \begin{pmatrix} \kappa_{1,1} & \kappa_{1,2} & \cdots & \kappa_{1,37} \\ \kappa_{2,1} & \kappa_{2,2} & \cdots & \kappa_{2,37} \\ \vdots & \vdots & \ddots & \vdots \\ \kappa_{37,1} & \kappa_{37,2} & \cdots & \kappa_{37,37} \end{pmatrix}. \tag{6}$$

Here we only consider the interlattice coupling with the same or adjacent wavevectors, as coupling strengths of the rest coupling are substantially smaller. Therefore, κ_{j_1,j_2} can be written as,

$$\kappa_{j_1,j_2} = \frac{2}{\sqrt{3}a^2} t(\mathbf{k}_{j_1} + \mathbf{G}_l^{(1)}) \begin{pmatrix} e^{i\mathbf{G}_m^{(2)}\cdot\boldsymbol{\tau}_A^{(2)}} & e^{i\mathbf{G}_l^{(1)}\cdot(\boldsymbol{\tau}_B^{(1)}-\boldsymbol{\tau}_A^{(1)})} e^{i\mathbf{G}_m^{(2)}\cdot\boldsymbol{\tau}_B^{(2)}} \\ e^{-i\mathbf{G}_l^{(1)}\cdot(\boldsymbol{\tau}_B^{(1)}-\boldsymbol{\tau}_A^{(1)})} e^{i\mathbf{G}_m^{(2)}\cdot\boldsymbol{\tau}_A^{(2)}} & e^{i\mathbf{G}_m^{(2)}\cdot\boldsymbol{\tau}_B^{(2)}} \end{pmatrix},$$
$$\text{when } \mathbf{k}_{j_2} = \mathbf{k}_{j_1} + (\mathbf{G}_l^{(1)} - \mathbf{G}_l^{(2)}) - \mathbf{G}_m^{(2)},$$

in which $\mathbf{G}_{l,m}^{(1,2)}$ can be taken as $\mathbf{0}$, and $\pm\mathbf{G}_1^{(1,2)}$, $\pm\mathbf{G}_2^{(1,2)}$ and $\pm\mathbf{G}_3^{(1,2)}$, and $\mathbf{G}_{1,2,3}^{(1,2)}$ are the three reciprocal lattice vectors of the first and second set of lattices, respectively. $t(\mathbf{k})$ is the Fourier transform of the distance-dependent coupling strength between Wannier functions.

We proceed by solving the eigenequation to obtain the eigenfrequencies and the eigenfunctions of the flatband modes. Supplementary Information Fig. 2 shows the momentum distribution and real-space pattern of a dipole flatband mode in the moiré superlattice at 9.43°, which has been analytically solved. In Extended Data Fig. 9, we perform three-dimensional full-wave simulations on this structure to obtain comprehensive properties of flatband modes. Achieving a flatband at the large twisted angle of 9.43° necessitates a stronger interlayer coupling strength. To this end, we fabricate the moiré superlattice by introducing two sets of twisted photonic graphene lattices into the same semiconductor membrane. The interlayer coupling strength of the system is maximized owing to the complete overlap of wavefunctions between the two photonic graphene lattices in the transverse dimension, as compared with two separated photonic graphene lattices with a twist. As a result, flatband and corresponding localized Bloch modes can be achieved in this device.

Full-wave simulation

We conduct three-dimensional full-wave simulations using the finite-element method to obtain the band structure and flatband eigenmodes of moiré superlattices. To simulate the band structure, we apply periodic boundary conditions to a single unit cell of the moiré superlattice, allowing us to obtain dispersion relations and field distributions of Bloch modes. To compute the eigenmode of a finite-sized cavity, we use scattering boundary conditions with perfectly matched layers as the boundary condition. The semiconductor membrane is set to have a refractive index of 3.45 + 0.0065i. During eigenmode simulations, we use a static imaginary part within the refractive index of the gain medium to simulate pump-induced gain within the cavity.

The reconfigurable cavity modes, including P-shaped, K-shaped and U-shaped cavity modes, fundamental and higher-order spatial modes, as well as single moiré unit cell cavity mode, are simulated by introducing Gaussian-profiled refractive index modulations (Δn) induced by optical pumping to the constituent local nanocavities (Supplementary Information Fig. 10). The peak value of the real part of refractive-index modulations is in the range −0.012 to −0.025, whereas that of the imaginary part is between −0.007 and −0.015 to achieve a simulated pattern that matches experimental results. For the simulation of the U-shaped cavity mode, the refractive index modulation peak value at the bottom is approximately 20% higher than that at the top. The introduced real part of the refractive index variation (Δn) during lasing is insufficient for localizing the light field for lasing. Moreover, the wavelength shift induced by Δn is only 4.1 to 8.6 nm, which is substantially smaller than the bandwidth of the flatband (about 19.3 nm). Therefore, the flatband-induced localization condition remains preserved throughout the lasing process. The mode volume of a cavity is calculated by $V_{\mathrm{mode}} = \frac{\int \mathrm{Re}[n(\mathbf{r})^2]\,|E(\mathbf{r})|^2\,\mathrm{d}^3\mathbf{r}}{\max[\mathrm{Re}[n(\mathbf{r})^2]\,|E(\mathbf{r})|^2]}$, in which $n(\mathbf{r})$ and $E(\mathbf{r})$ are the local refractive index and electric field intensity, respectively.

Optical characterization

We use a pulsed laser (wavelength 1,064 nm; pulse width, 5 ns; repetition rate, 12 kHz) to excite the device at ambient temperature. A custom-built microscopy system integrated with near-infrared CCD and spectrometer is used for characterizing the emission properties of the nanolaser arrays, in which both excitation and emission beams are collected by a common objective lens (100×, numerical aperture = 0.82). The spectrometer has a resolution of about 0.1 nm. Masks are used in the excitation path to shape it, whereas spatial filters are used in the collection path to obtain spatially resolved spectra and emission patterns. The second-order intensity correlation function $g^{(2)}(\tau)$ is obtained using a Hanbury Brown and Twiss experimental set-up, in which a pulsed laser with 1 MHz repetition rate is used as the pump source (wavelength 1,064 nm; pulse width 0.2 ns).

Reporting summary

Further information on research design is available in the Nature Portfolio Reporting Summary linked to this article.

Data availability

We declare that the data supporting the findings of this study are available in the paper.

Acknowledgements This work is supported by the National Key R&D Program of China (grant nos. 2018YFA0704401 and 2022YFA1404700), the National Natural Science Foundation of China (grant nos. 12225402, 91950115, 11774014 and 62321004), the Beijing Natural Science Foundation (Z180011) and the New Cornerstone Science Foundation through the XPLORER PRIZE. The authors thank Peking Nanofab and the National Center for Nanoscience and Technology for fabrication assistance.

Author contributions R.-M.M. conceived the concept and supervised the project. H.-Y.L., Y.-H.O. and W.-Z.M. carried out numerical simulations and performed optical characterization. Z.-W.Z. and W.-Z.M. fabricated the devices. R.-M.M., H.-Y.L. and Y.-H.O. performed the data analysis. R.-M.M. wrote the manuscript.

Competing interests The authors declare no competing interests.

Additional information
Supplementary information The online version contains supplementary material available at https://doi.org/10.1038/s41586-023-06789-9.
Correspondence and requests for materials should be addressed to Ren-Min Ma.
Peer review information *Nature* thanks the anonymous reviewers for their contribution to the peer review of this work.

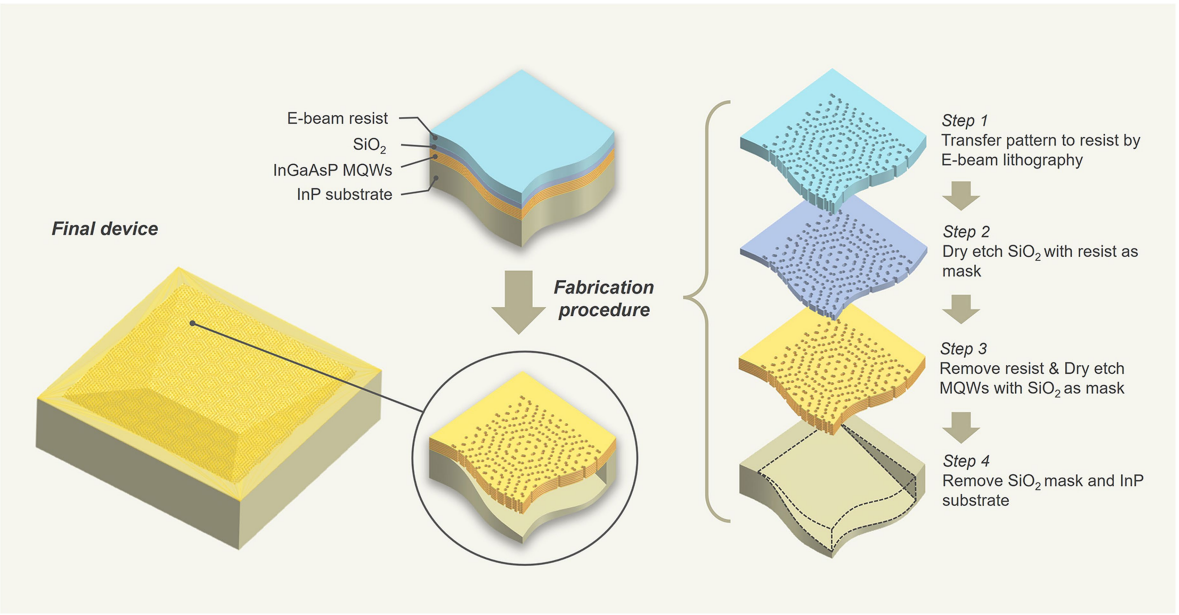

Extended Data Fig. 1 | Fabrication procedure of the reconfigurable moiré nanolaser array. The semiconductor membrane for moiré superlattice fabrication consists of InGaAsP MQWs with a thickness of 200 nm. The fabrication procedure includes four essential steps. Step 1: transferring pattern to resist by electron-beam lithography. Step 2: dry etching SiO_2 by means of ICP, in which resist is used as mask. Step 3: dry etching MQWs through ICP, in which patterned SiO_2 is used as mask. Step 4: removing SiO_2 mask and InP substrate using wet-etching methods.

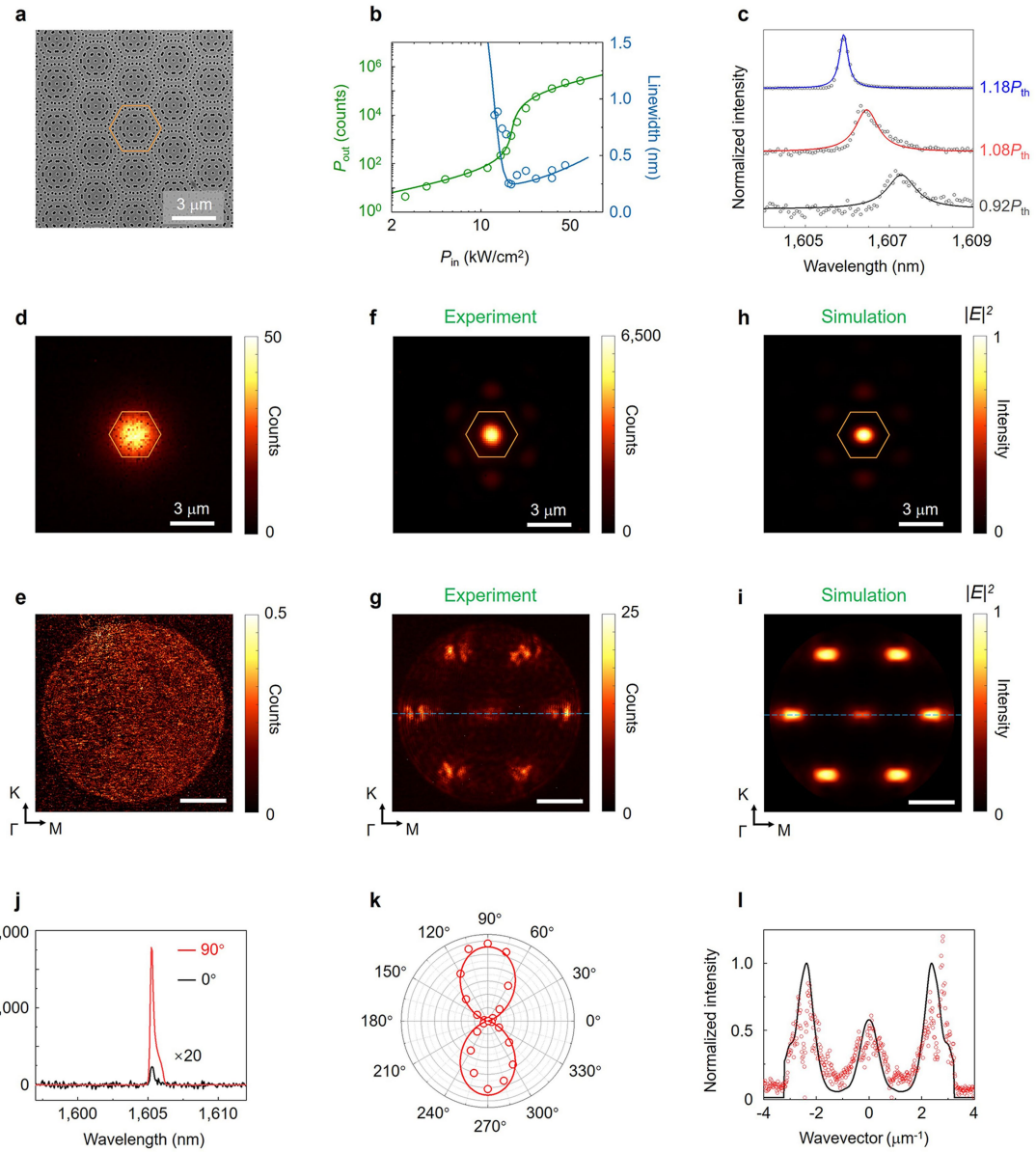

Extended Data Fig. 2 | Nanolasing in a single unit cell of the moiré superlattice. a, SEM image of the device. The orange hexagon highlights the single unit cell of the moiré superlattice for nanolasing. **b**, Light–light curve (green) and linewidth evolution curve (blue) of the single-cavity nanolaser. Circles, data; lines: guides to the eye. **c**, Normalized emission spectra near lasing threshold (P_{th}), which shows the linewidth narrowing of the lasing mode. Circles, data; lines, fitting. **d**,**e**, Spontaneous emission patterns of the device in real (**d**) and momentum (**e**) spaces. **f**,**g**, Lasing emission patterns in real (**f**) and momentum (**g**) spaces. **h**,**i**, Simulated emission patterns in real (**h**) and momentum (**i**) spaces. The lasing flatband mode exhibits a narrower bandwidth along the Γ–M (horizontal) direction compared with that along the Γ–K (vertical) direction (Extended Data Fig. 9), resulting in a more localized mode along the Γ–M direction (**h**). Consequently, this leads to a broader momentum distribution (**i**) according to Fourier transform. **j**, Polarization-resolved lasing emission spectra. The spectrum counts at 0° polarization are magnified by a factor of 20. **k**, Normalized lasing emission intensity as a function of the polarization angle. **l**, Intensity profiles along the dashed lines in **g** and **i**. Scale bars, 1.6 μm^{-1} (**e**,**g**,**i**).

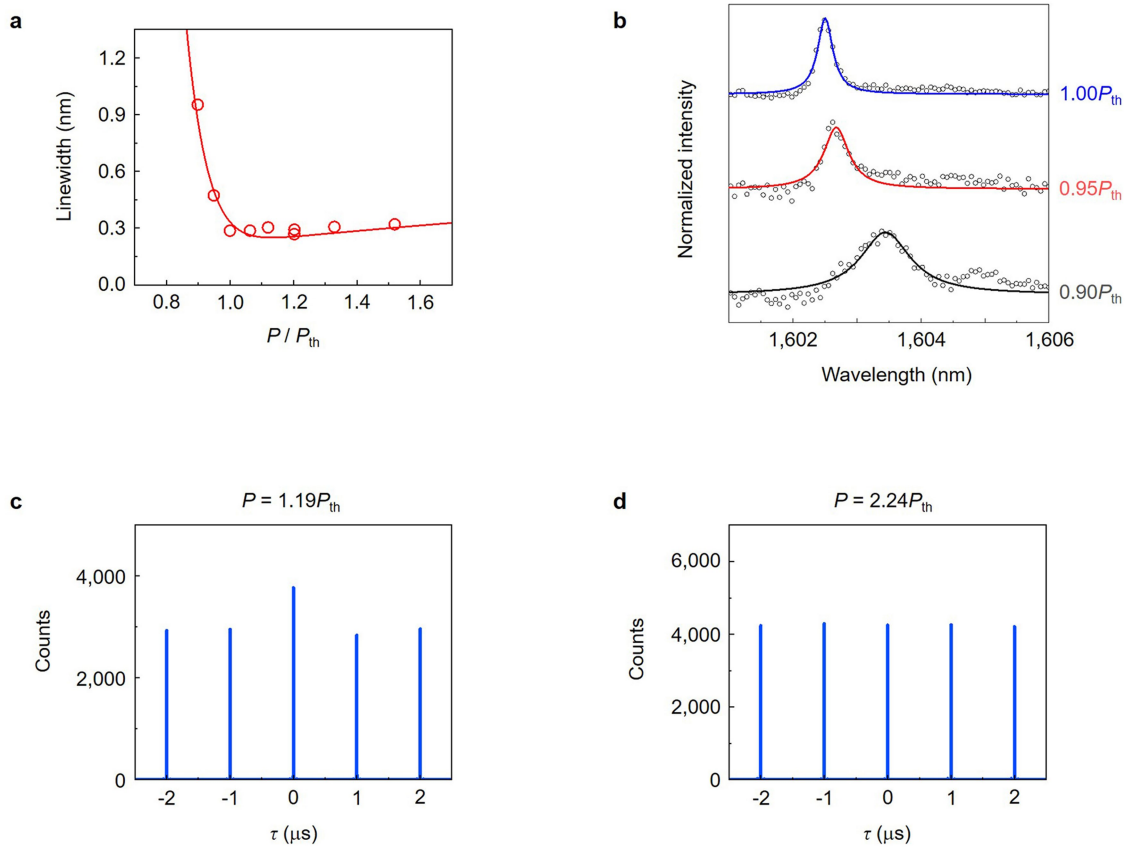

Extended Data Fig. 3 | Linewidth narrowing and photon emission statistics transition of the U-shaped moiré nanolaser array. a, Linewidth evolution curve of the U-shaped moiré nanolaser array. P_{th}, lasing threshold; circles, data; line, guide to the eye. **b**, Normalized emission spectra near the lasing threshold (P_{th}), which shows the linewidth narrowing of the lasing mode. Circles, data; lines, fitting. **c**,**d**, Second-order intensity correlation function $g^{(2)}(\tau)$ of the nanolaser array at $1.19P_{th}$ (**c**) and $2.24P_{th}$ (**d**). Near the lasing threshold (**c**), the emitted photons exhibit super-Poissonian light characteristics ($g^{(2)}(\tau = 0) > 1$). Above the lasing threshold (**d**), the photon emission statistics transition from super-Poissonian to Poissonian, indicating the emergence of coherent light emission ($g^{(2)}(\tau = 0) = 1$).

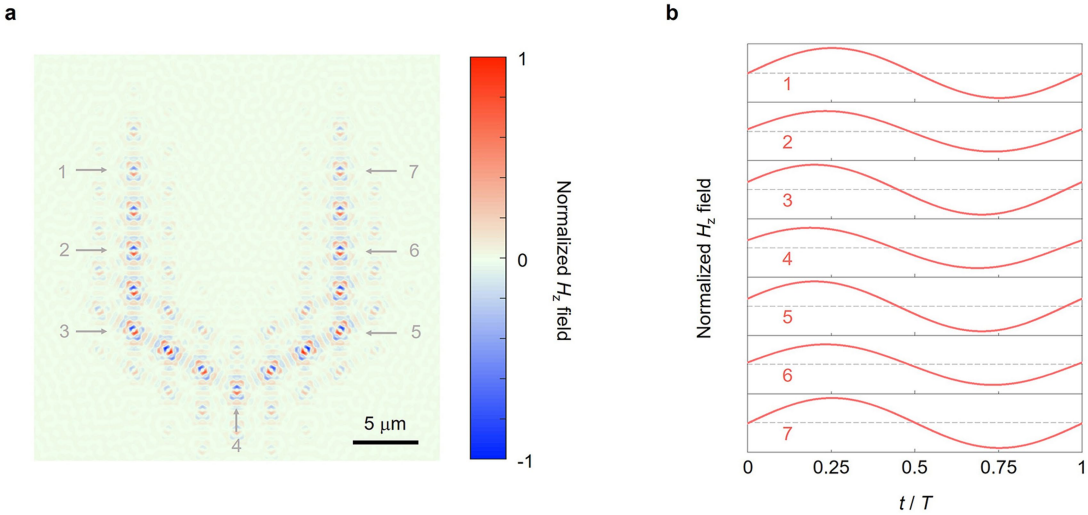

Extended Data Fig. 4 | Phase distribution of the U-shaped moiré nanolaser obtained by three-dimensional full-wave simulation. a, H_z field pattern of the U-shaped moiré nanolaser array. **b**, Time-resolved H_z field at the seven unit cells marked in **a**, indicating that all of them oscillate in phase. t, time; T, oscillation period.

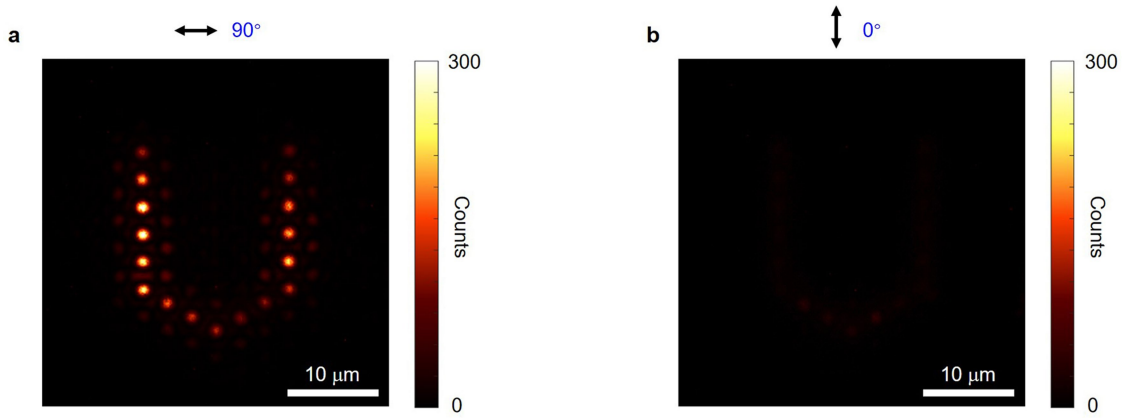

Extended Data Fig. 5 | Uniform emission polarization among all constituent nanolasers in the U-shaped nanolaser array. a, Polarization-resolved lasing pattern of the U-shaped nanolaser array with a polarizer filter oriented at 90°. **b**, Polarization-resolved lasing pattern of the U-shaped nanolaser array with a polarizer filter oriented at 0°.

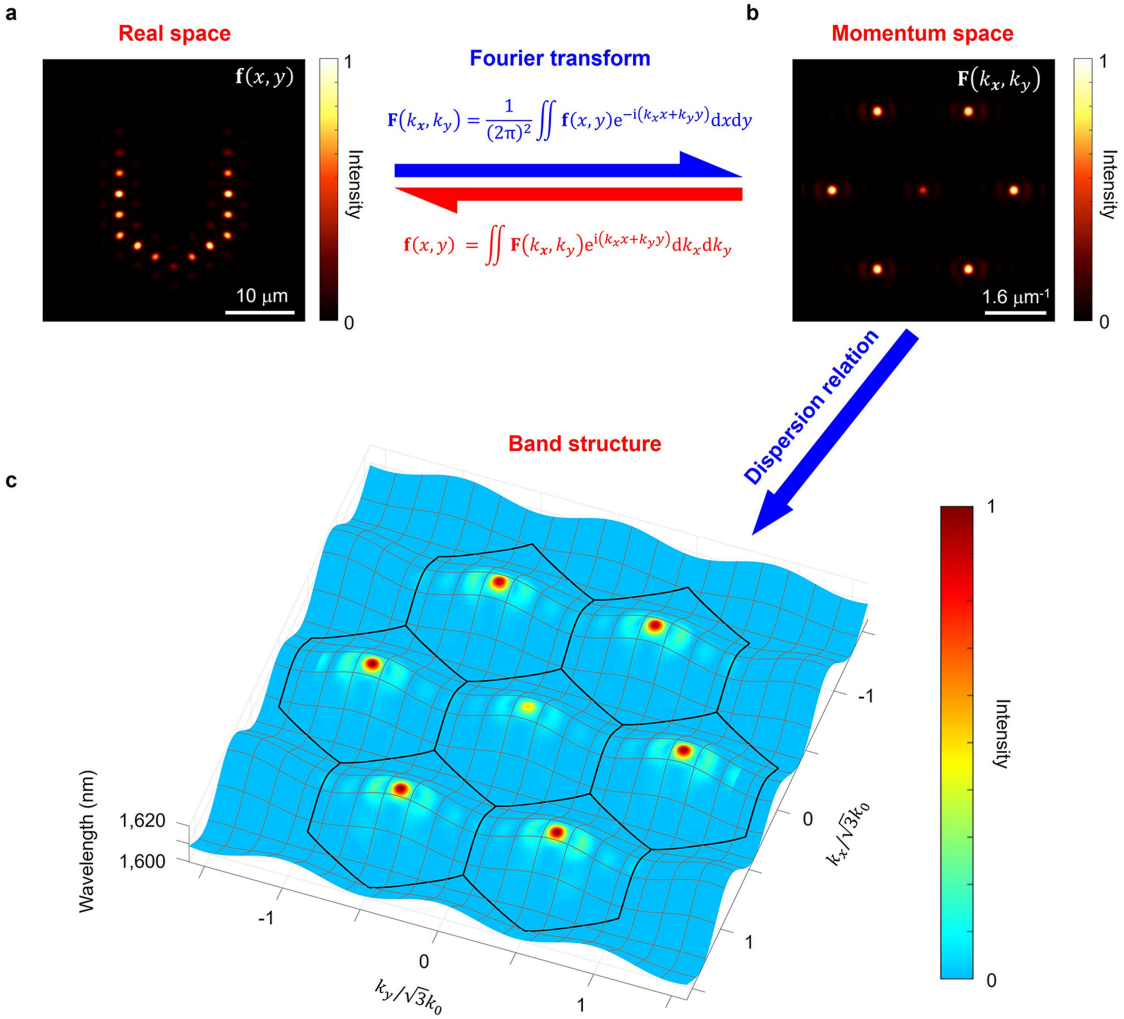

Extended Data Fig. 6 | The relationship between patterns in real space, patterns in momentum space and the presence of flatband modes. **a**, Simulated pattern of U-shaped nanolaser array observed in real space. **b**, Simulated pattern of U-shaped nanolaser array observed in momentum space. The patterns in **a** and **b** can be mutually transformed through Fourier transform. **c**, Band diagram superimposed with the momentum-space pattern depicted in **b**, which shows the eigenfrequency distribution of the lasing mode of the U-shaped nanolaser array determined by the dispersion relation.

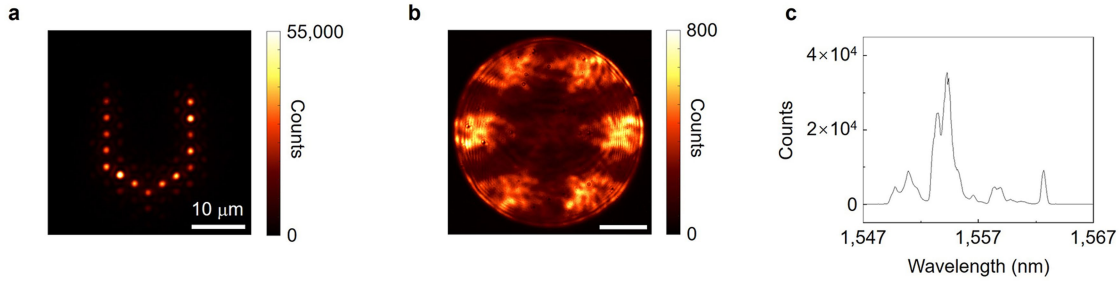

Extended Data Fig. 7 | U-shaped nanolaser array emitting without phase locking. a,**b**, Lasing emission patterns of U-shaped nanolaser array emitting without phase locking in real (**a**) and momentum (**b**) space. Despite the U shape being well maintained in real space, the emission exhibits strong divergence in momentum space resulting from the lack of phase locking. Scale bar, 1.6 μm^{-1} (**b**). **c**, Corresponding lasing spectrum of the U-shaped nanolaser array emitting without phase locking.

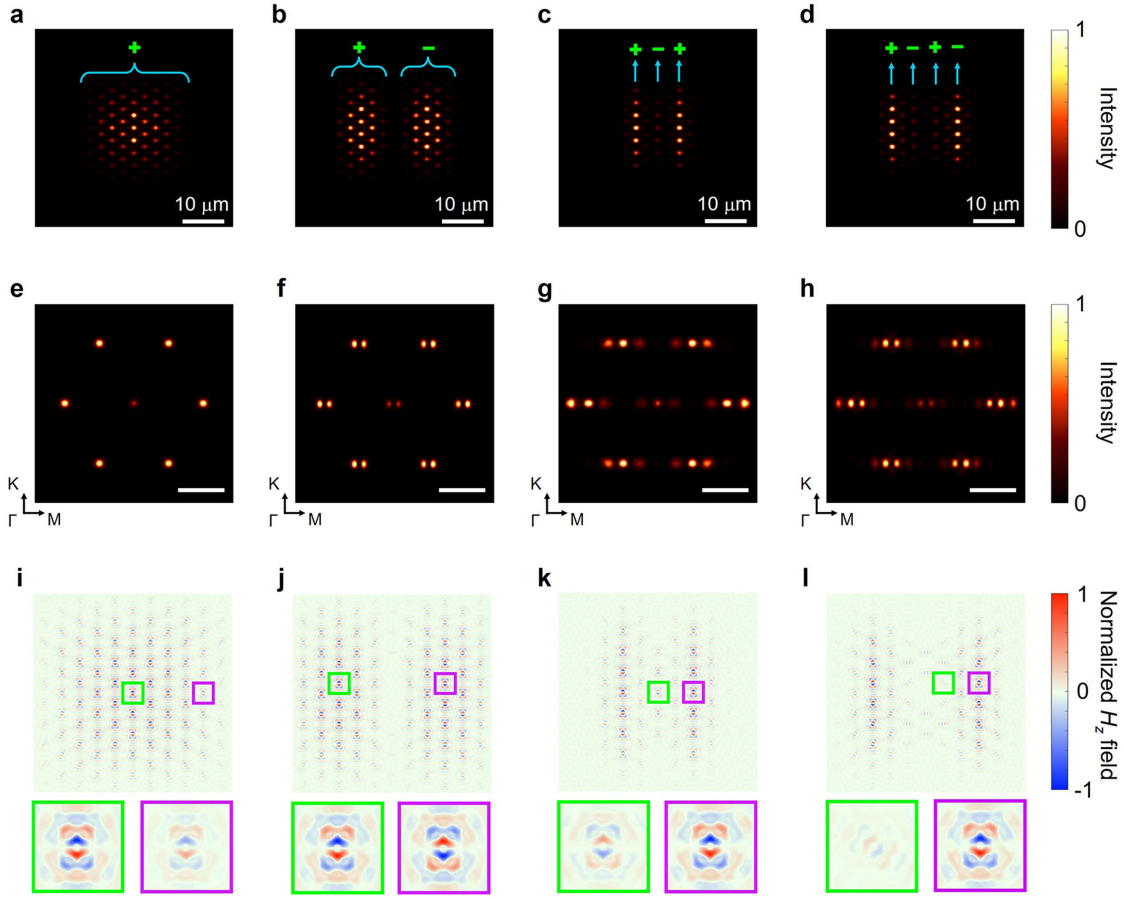

Extended Data Fig. 8 | Simulated patterns of the fundamental, first higher, second higher and third higher modes. a–**d**, Simulated real-space patterns of the fundamental (**a**), first higher (**b**), second higher (**c**) and third higher (**d**) modes. **e**–**h**, Simulated momentum-space patterns of the fundamental (**e**), first higher (**f**), second higher (**g**) and third higher (**h**) modes. **i**–**l**, H_z field phase distributions of the fundamental (**i**), first higher (**j**), second higher (**k**) and third higher (**l**) modes. Insets in **i**–**l**, enlarged phase distributions in marked areas. In the fundamental mode, all constituent local nanocavities exhibit synchronized in-phase oscillation. In the higher-order modes, there exists a phase difference of π between any two adjacent regions separated by a node (intensity zero crossing). Scale bars, 1.6 μm^{-1} (**e**–**h**).

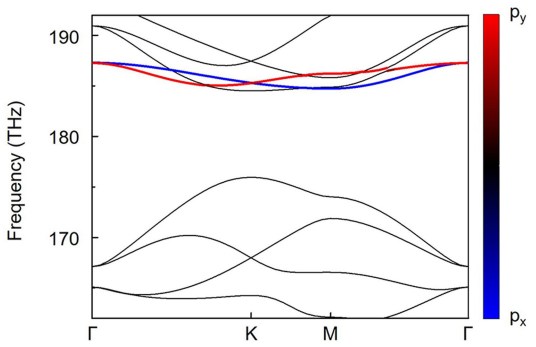

Extended Data Fig. 9 | Three-dimensional full-wave-simulated band structure of the moiré nanolaser array. The red and blue bands represent two dipole flatbands. The colour bar represents the corresponding weight of a flatband mode in two polarizations, namely, p_x and p_y.

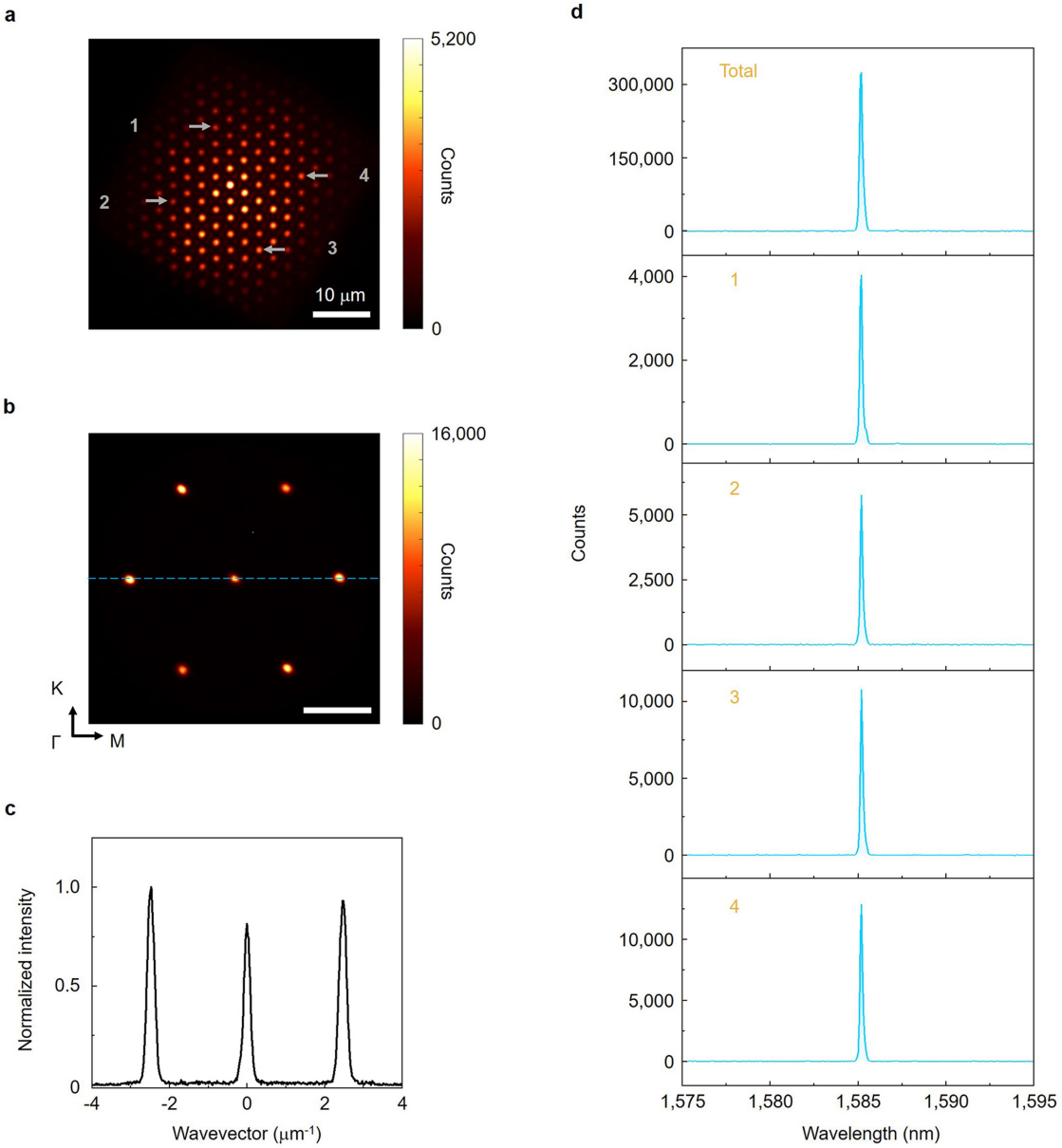

Extended Data Fig. 10 | Scalability of the moiré nanolaser array. a,**b**, Real (**a**) and momentum (**b**) spaces lasing patterns of the large-scale moiré nanolaser array on SiO_2 substrate. Scale bar, 1.6 μm^{-1} (**b**). **c**, Intensity profile along the dashed line in **b**. **d**, Spectrum of the entire moiré nanolaser array (top spectrum) and spatially resolved spectra from four individual unit cells marked in **a**.

nature research

Corresponding author(s): Ren-Min Ma

Lasing Reporting Summary

Nature Research wishes to improve the reproducibility of the work that we publish. This form is intended for publication with all accepted papers reporting claims of lasing and provides structure for consistency and transparency in reporting. Some list items might not apply to an individual manuscript, but all fields must be completed for clarity.

For further information on Nature Research policies, including our data availability policy, see Authors & Referees.

Experimental design

Please check: are the following details reported in the manuscript?

1. Threshold

Plots of device output power versus pump power over a wide range of values indicating a clear threshold	☒ Yes ☐ No	Fig. 2d, Extended Data Fig. 2b, Supplementary Information Figs. S7a,c.

2. Linewidth narrowing

Plots of spectral power density for the emission at pump powers below, around, and above the lasing threshold, indicating a clear linewidth narrowing at threshold	☒ Yes ☐ No	Extended Data Fig. 2b,c, Extended Data Figs. 3a,b, Supplementary Information Fig. S7.
Resolution of the spectrometer used to make spectral measurements	☒ Yes ☐ No	Optical characterization of Methods section.

3. Coherent emission

Measurements of the coherence and/or polarization of the emission	☒ Yes ☐ No	The coherent emission is verified by measuring second-order intensity correlation (g(2)), where the results are shown in Fig. 2d, Extended Data Figs. 3c,d.

4. Beam spatial profile

Image and/or measurement of the spatial shape and profile of the emission, showing a well-defined beam above threshold	☒ Yes ☐ No	Figs. 2g,h, Figs. 3c,d,j,k, Figs. 4a-h, Figs. 5a,b,d,e, Extended Data Fig. 2f, Extended Data Fig. 7a, Supplementary Information Fig. S9d, Extended Data Figs. 10a,b.

5. Operating conditions

Description of the laser and pumping conditions *Continuous-wave, pulsed, temperature of operation*	☒ Yes ☐ No	Optical characterization of Methods section
Threshold values provided as density values (e.g. W cm^{-2} or J cm^{-2}) taking into account the area of the device	☒ Yes ☐ No	Fig. 2d and related discussion

6. Alternative explanations

Reasoning as to why alternative explanations have been ruled out as responsible for the emission characteristics *e.g. amplified spontaneous, directional scattering; modification of fluorescence spectrum by the cavity*	☒ Yes ☐ No	We have systematically studied the lasing properties of our devices in experiment and in theory. These results are shown throughout the manuscript and the Supplementary Information. The phase transition from spontaneous emission to lasing emission is verified by well defined lasing threshold, pattern, linewidth narrowing and the photon emission statistics transition from super-Poissonian to Poissonian, which rules out other alternative explanations.

7. Theoretical analysis

Theoretical analysis that ensures that the experimental values measured are realistic and reasonable *e.g. laser threshold, linewidth, cavity gain-loss, efficiency*	☒ Yes ☐ No	Figs. 2i,j, Figs. 3e,f,l,m, Supplementary Information Fig. S2, Extended Data Figs. 2h,i, Supplementary Information Fig. S3, Extended Data Fig. 4, Extended Data Fig. 8, Extended Data Fig. 9.

8. Statistics

Number of devices fabricated and tested	☒ Yes ☐ No	We have fabricated and tested over 100 lasing devices. Typical devices are shown in Figs. 2-5, Extended Data Fig. 2, Extended Data Fig. 7, Supplementary Information Fig. S9, Extended Data Fig. 10.

Statistical analysis of the device performance and lifetime (time to failure)	☒ Yes ☐ No	We have fabricated and tested over 100 lasing devices. All the lasing devices show similar performance. Our devices are based on III-V semiconductor, they did not show performance degradation during the test period of over a year.